NANO · MICRO small
www.small-journal.com

Synergistically Engineered All Van der Waals GaS–WSe_2 Photodiodes: Approaching Near-Unity Polychromatic Linearity for Multifunctional Optoelectronics

*Tawsif Ibne Alam, Sumaiya Umme Hani, Zongliang Guo, Safayet Ahmed, Ahmed Mortuza Saleque, Md. Nahian Al Subri Ivan, Shuvra Saha, and Yuen Hong Tsang**

Van der Waals (vdW) heterojunctions represent a significant frontier in post-Moore era optoelectronics, especially in optimizing photosensor performance through multivariate approaches. Here synergistic engineering of GaS–WSe_2 all-vdW photodiodes is investigated, which exhibit broadband detection (275–1064 nm), multispectral unity approaching linearity, alongside a substantial linear dynamic range (LDR) of 106.78 dB. Additionally, the photodiodes achieve a remarkable on/off ratio of 10^5 and rapid response edges of 545/471 µs under a 405 nm pulsed source, exhibiting ultralow light detection capabilities (dark currents ~fA), culminating in a peak responsivity of 376.78 mA W^{-1} and a detectivity of 4.12×10^{11} Jones under 450 nm illumination, complemented by an external quantum efficiency (EQE) of 30% and a fill factor of ≈0.33. Based on the analysis of multiple all-vdW devices, the importance of Fermi-level pinning free metal–2D interface engineering that enables effective modulation of the Schottky barrier height via vdW metal contacts is highlighted and meticulous thickness-engineered layers in developing a robust depletion region within the type-II GaS–WSe_2 heterojunction are employed, ultimately achieving a favorable balance among photocarrier generation recombination, separation, transport, and extraction. This comprehensive investigation sets the stage for future developments in critically engineered next-generation vdW optoelectronic devices.

1. Introduction

Low-dimensional van der Waals (vdW) materials (vdW-m) with intrinsically passivated basal planes have been at the forefront of investigation over the last two decades, due to their perceived future dominance in the post-Moore era of optoelectronics. With the ease of access to fabrication of atomically thin vdW heterojunctions having clean interfaces for prototypical demonstration, a substantial amount of research has been ongoing to establish their potential in multifunctional optoelectronics. Among them, transitional metal dichalcogenides (TMDC) and metal monochalcogenides are equally imperative vdW-m for optoelectronic-sensing applications, due to enhanced light–matter interaction, high charge carrier mobility, layer-dependent tunable bandgaps, all in the ultrathin regime of few atomic layers.[1,2] GaS, a layered post-transition metal monochalcogenide, has demonstrated excellent light–matter interaction in the ultraviolet–visible

T. I. Alam, S. U. Hani, Z. Guo, M. N. A. S. Ivan, S. Saha, Y. H. Tsang
Department of Applied Physics
Materials Research Center
Photonics Research Institute
and Research Institute for Advanced Manufacturing
The Hong Kong Polytechnic University
Hung Hom, Kowloon, Hong Kong 999077, P. R. China
E-mail: yuen.tsang@polyu.edu.hk

The ORCID identification number(s) for the author(s) of this article can be found under https://doi.org/10.1002/smll.202410841

DOI: 10.1002/smll.202410841

T. I. Alam, S. U. Hani, Z. Guo, M. N. A. S. Ivan, S. Saha, Y. H. Tsang
Shenzhen Research Institute
The Hong Kong Polytechnic University
Shenzhen, Guangdong 518057, China

S. Ahmed
Department of Physics
Oregon State University
Corvallis, OR 97331, USA

A. M. Saleque
Physical Science and Engineering Division
King Abdullah University of Science and Technology
Thuwal 23955, Saudi Arabia

regime.[3] Its remarkable structural[4] and phonon dynamics characteristics[5] suggest promising applications in flexible optoelectronics. However, the reported low intrinsic in-plane mobility has hindered its progress in realizing in-plane self-powered photosensors, till date. Earlier it was suggested that ultrathin films of gallium monochalcogenides could be suitable active element candidates for ultraviolet photon harvesting in vertical tunneling transistors.[6] Besides, double peak valence band maxima, as theoretically predicted for ultrathin GaS, encourage photoabsorption,[3] making them suitable for optoelectronic heterojunction devices. Thus far, reported photoconductive-type bare GaS,[7,8] defect-based GaS devices[7] and heterojunction devices like Gr–GaS–Gr[8] and GaS–WS_2[9] required large operating voltages and demonstrated sluggish response speeds, necessitating renewed investigation into favorable layer thickness determination, device structure, and contact engineering approaches, conducive to self-powered applications and faster response speeds. It is well established that self-powered heterojunction optoelectronics benefits from type-II heterointerface facilitating band bending and enhanced charge-carrier separation.[10] However, shifting of the band edges and Fermi level owing to impetuous layer thickness modification and emergence of refractory Schottky barrier at the contact regions due to Fermi-level pinning (FLP) could nullify these type-II junction benefits. Additionally, despite the intrinsic passivation of their basal planes, vdW-material-based photodiodes, even with optimized approaches, typically exhibit a power exponent α of ≈0.9. This indicates the presence of recombination and trapping processes; however, the underlying causes have yet to be fully elucidated. The ideal value of $\alpha = 1$ has thus far remained an unrealistic target, with any value approaching 1 considered satisfactory. To achieve a value closer to 1, a well-optimized strategy must be developed, alongside a renewed focus on understanding the bottlenecks that influence α. While many assume that defects within the semiconductor are the primary sources of recombination and trapping, there has been comparatively little attention given to the role of contact regions. This is especially critical for large-bandgap vdW materials like GaS and its heterojunctions, which have not yet been thoroughly investigated. In the context of transistor applications involving vdW materials and their heterojunctions, where charge injection is critical, the contact regions have been identified as significant bottlenecks due to issues such as FLP, large Schottky barriers, and elevated contact resistance. This raises the question of the role that FLP plays in the performance of vdW photodiodes, particularly when metal-induced gap states arise as a consequence of FLP. If an ideally optimized vdW photodiode is achieved without recombination or trapping occurring in the semiconductor and contact regions, can we attain $\alpha = 1$?

The selection of number of layers is subjective to the applications of the constituent material and may not be universal for every aspect; however, a clear strategy has been already adopted for FLP free application of vdW-m, owing to recent investigation of vdW transfer metal contacts for efficient current injection in field-effect transistors (FETs)[11–14] and photocarrier extraction in solar cells.[15] Hence, with meticulous engineering strategy, we report a photovoltaic type-II, all van der Waals GaS–WSe_2 heterojunction photodetector, having thickness, structure, and FLP resilience optimization of contacts to achieve near-unity polychromatic linearity, large linear dynamic range (LDR), broadband photovoltaic responsivity with fast response speeds, and high quantum efficiency with a name coined "all van der Waals" (a-vdW) due to the integration of the metal contacts with intimate vdW interaction. Moreover, our systematic investigation on multiple a-vdW devices along with a control device fabricated using traditional electron beam lithography (EBL) pattered contacts for comparison, covering key performance attributes such as junction potentials, electronic–optoelectronic characteristics, further endorse, and emphasize the need of meticulous approaches to be undertaken for reaching an optimum balance among photocarrier generation, recombination, separation, transport, and extraction, based on adjusting GaS–WSe_2 layer thicknesses, device structure, and integration strategy of metal contacts to achieve such high performance for multifunctional applications.

2. Results and Discussion

2.1. Device Structure and Characterization of WSe_2–GaS Heterostructure

Figure 1a,b illustrates the schematic of the WSe_2–GaS vdW heterostructure and an optical microscopic image of an a-vdW photodiode. The fabrication process consists of two distinct steps: the fabrication of the heterojunction and the integration of the vdW metal contacts. First, h-BN was exfoliated onto a silicon substrate with a 300 nm oxide layer. WSe_2 and GaS of appropriate thicknesses were also exfoliated and identified using an optical microscope and were subsequently transferred onto the h-BN layer using a dry transfer technique. h-BN was chosen as the dielectric material to provide potential screening from charged impurities and adsorbates on the SiO_2 surface,[16] which could modulate the carrier-transport characteristics[17] and influence the Schottky barrier height between the contacts and the underlying vdW-m.[18] Hence this optimized design sequentially stacks h-BN, WSe_2 , and GaS layers with precise alignment transfer stage. In the second step, vdW integration of Ag/Au (38 nm/22 nm) contacts was achieved through a modified transfer method using prefabricated contacts on a sacrificial substrate (for further details on the fabrication process, refer to Section S1 in the Supporting Information). This approach minimizes FLP and enhances photocarrier extraction.

To better understand the layer-coupling properties of the prepared heterostructure photodiode, we employed Raman spectroscopy, as shown in Figure 1c. For few-layer GaS, the prominent vibrational modes A^1_{1g} and A^2_{1g} were identified at 188.16 and 359.58 cm^{-1}, respectively, while the less prominent E^1_{2g} mode appeared at 296.01 cm^{-1}, consistent with previous reports.[19] Likewise, few-layer WSe_2 exhibited a prominent in-plane mode E^1_{2g} at 249.58 cm^{-1} and a weak out-of-plane A_{1g} mode at 256.94 cm^{-1}.[20,21] In the overlapped region between WSe_2 and GaS, all peaks corresponding to the individual layers were observed, indicating a high-quality heterojunction. Moreover, to further investigate the charge-transfer characteristics and coupling effects, we performed Raman intensity mapping and analyzed the photoluminescence (PL) spectra and mapping. As shown in the Raman intensity mapping for the peaks at 256.94 cmand 359.58 cm^{-1} in Figure 1d, we observed a notable reduction in Raman intensity—a phenomenon known as "Raman quench"—

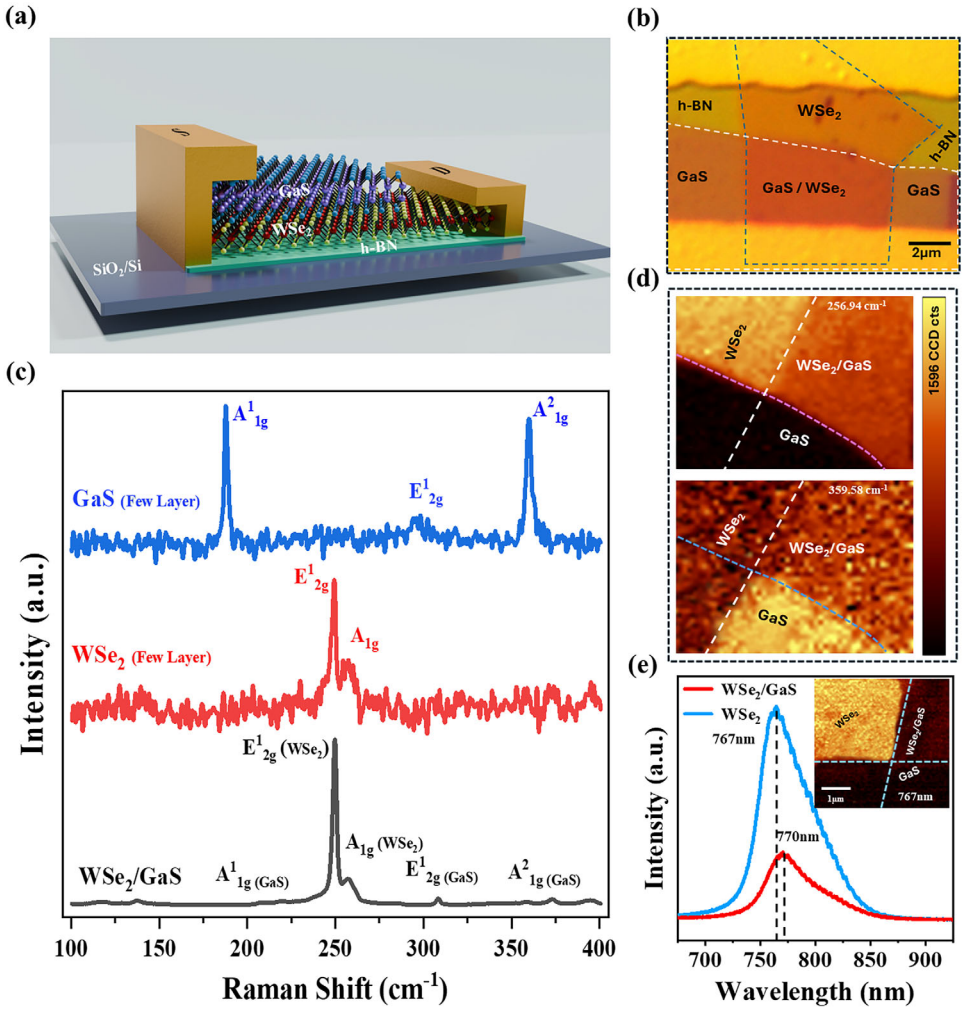

Figure 1. a) Schematic Illustration of all van der Waals heterojunction photodetector (purple and red spheres represent gallium and tungsten metal atoms, while blue and yellow spheres represent sulfur and selenium atoms, respectively). b) Optical microscopic image of the device. c) Raman spectroscopy of few-layer GaS showing characteristics $A^1{}_{1g}$, $E^1{}_{2g}$, and $A^2{}_{1g}$ modes, ultrathin WSe_2 showing characteristics $E^1{}_{2g}$ and A_{1g} modes, and the heterojunction region showing all the characteristics peaks. d) Raman mapping of A_{1g} mode (256.94 cm^{-1}) of WSe_2 (top) and $A^2{}_{1g}$ (359.58 cm^{-1}) of GaS, showing evident uniform Raman quenching in the overlapped regions for both the modes. e) Photoluminescence spectroscopy of ultrathin WSe_2 in the bare and overlapped regions of the heterojunction, with the inset showing the PL mapping. Evident PL quenching is observed from both the spectroscopy and mapping results.

which signifies strong interfacial coupling between the GaS and WSe_2 flakes.[16,22] The PL spectra in Figure 1e reveal strong excitonic emission for bare WSe_2, while an obviously quenched PL spectrum is observed in the overlapping region. Furthermore, the intensity mapping shown in Figure 1e (inset) demonstrates uniform quenching effects of PL intensity in the heterointerface region, indicating nonradiative recombination in the GaS–WSe_2 heterostructure and efficient separation of photogenerated electron–hole pairs.[23] These results from Raman scattering and PL spectra indicate a well-coupled, pristine heterointerface suitable for photodetection mechanisms.

Atomic force microscopy (AFM) was employed to obtain the height profile of the prepared heterojunction photodetector, as shown in **Figure 2a**. The height profile analysis revealed the height of the GaS flake was ≈8.5 nm, (≈10 layers), while the WSe_2 flake had a height of around 3 nm, (≈4 layers), confirming the thicknesses of the layers used in constructing the heterojunction. To better understand the charge-transport characteristics, ultraviolet photoelectron spectroscopy (UPS) was employed to determine the complete energy level alignment before contact (Section S2, Supporting Information). The work functions (Φ) of GaS and WSe_2 were estimated to be 4.19 eV and 4.38 eV, respectively, calculated from the difference between the second electron cutoff energy and the photon energy of the He I light source (21.21 eV), as outlined in Section S2 and Figure S2a,b (Supporting Information). The valence band edges of GaS and WSe_2 were found to be 2.41 and 0.38 eV lower than their respective Fermi energies (E_f), as shown in the insets of those figures. Additionally, we employed Kelvin probe force microscopy (KPFM) to investigate the Fermi-level adjustments at the heterojunction (Figure 2b), revealing a surface potential difference (SPD) of ≈200 mV across the heterojunction (details of the calculation can be found in Section S3 in

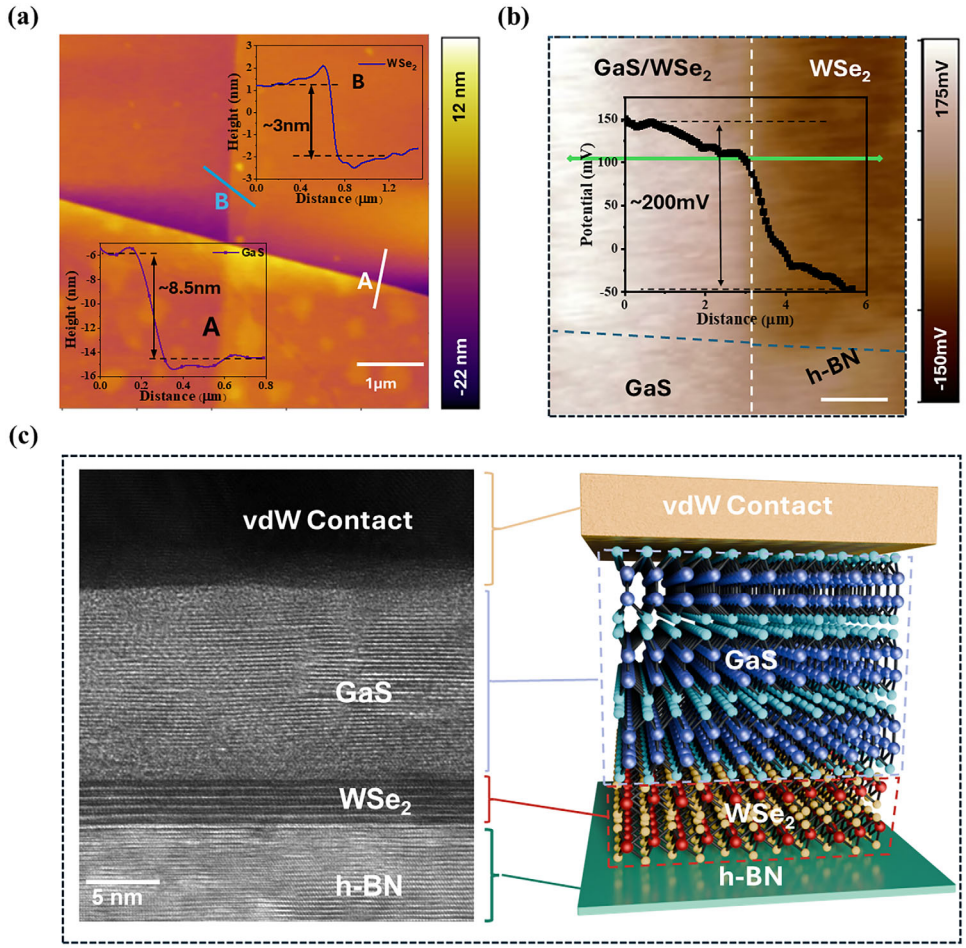

Figure 2. a) AFM image of the heterojunction region with corresponding height profiles showing a thickness of GaS and WSe_2 layer of 8.5 nm (region A) and 3 nm (region B), respectively. b) KPFM image of the heterojunction region with the corresponding SPD profile, showing an SPD of ≈200 mV. c) Cross-sectional HR-STEM image of the all-vdW region of the heterojunction, showing (from bottom) h-BN, WSe_2, GaS, and vdW contact, with pristine interfaces between constituent junctions.

the Supporting Information). Notably, the Fermi-level difference between WSe_2 and GaS, measured at around 0.19 eV from UPS measurements, closely matches the results obtained from KPFM. Combining the insights gained from KPFM and UPS, along with the reported bandgaps of 1.3 eV for few-layer WSe_2[24,25] and 2.5 eV for GaS,[26,27] the proposed type-II heterointerface band diagram is illustrated in Figure S2c (Supporting Information). Additionally, high-resolution scanning transmission electron microscopy (HR-STEM) was employed at the cross section of a device to verify the quality of a-vdW heterojunction region, as illustrated in Figure 2c. The investigated region consists of few-layer h-BN, ultrathin WSe_2 , few layers of GaS, encapsulated by vdW contact. The images reveal clean interfaces within the 2D–2D heterojunction, free of impurities, and the 2D–metal interface shows an undisturbed, column-like structure of the naturally passivated GaS layers, maintaining a vdW gap without any perforation of metal into the GaS layer. This suggests a clean metal–vdWm interface, which is conducive to FLP-free operation. Additionally, we utilized high-angle annular dark field (HAADF) STEM energy-dispersive X-ray spectroscopy (EDS) mapping to determine the elemental composition of the constituent elements at the 2D–2D interface (Section S4 and Figure S3, Supporting Information). The EDS results further complement the Raman and PL spectroscopic conclusions of a robust and pristine heterojunction, composed of GaS–WSe_2.

2.2. Electronic and Optoelectronic Characteristics of the GaS–WSe_2 a-vdW Photodiode

The charge-injection mechanism in a vdW materials' interface has significant impact on numerous performance descriptor figures of merit, including contact resistance, current on/off ratio, and response time of the device.[28] For vdW heterostructure devices, general approximation of the transport characteristics is well established within the framework of direct tunneling (DT) under the Simmons model at low bias, Fowler–Nordheim (FN) tunneling model at cold field emission regime, and space charge limited (SPCL) emission regime.[29] To elucidate the electronic transport in the heterojunction, the I_d–V_d characteristics for the device was obtained (**Figure 3a–c**). Drain voltage with positive polarity was applied to the WSe_2 side, while the source terminal at

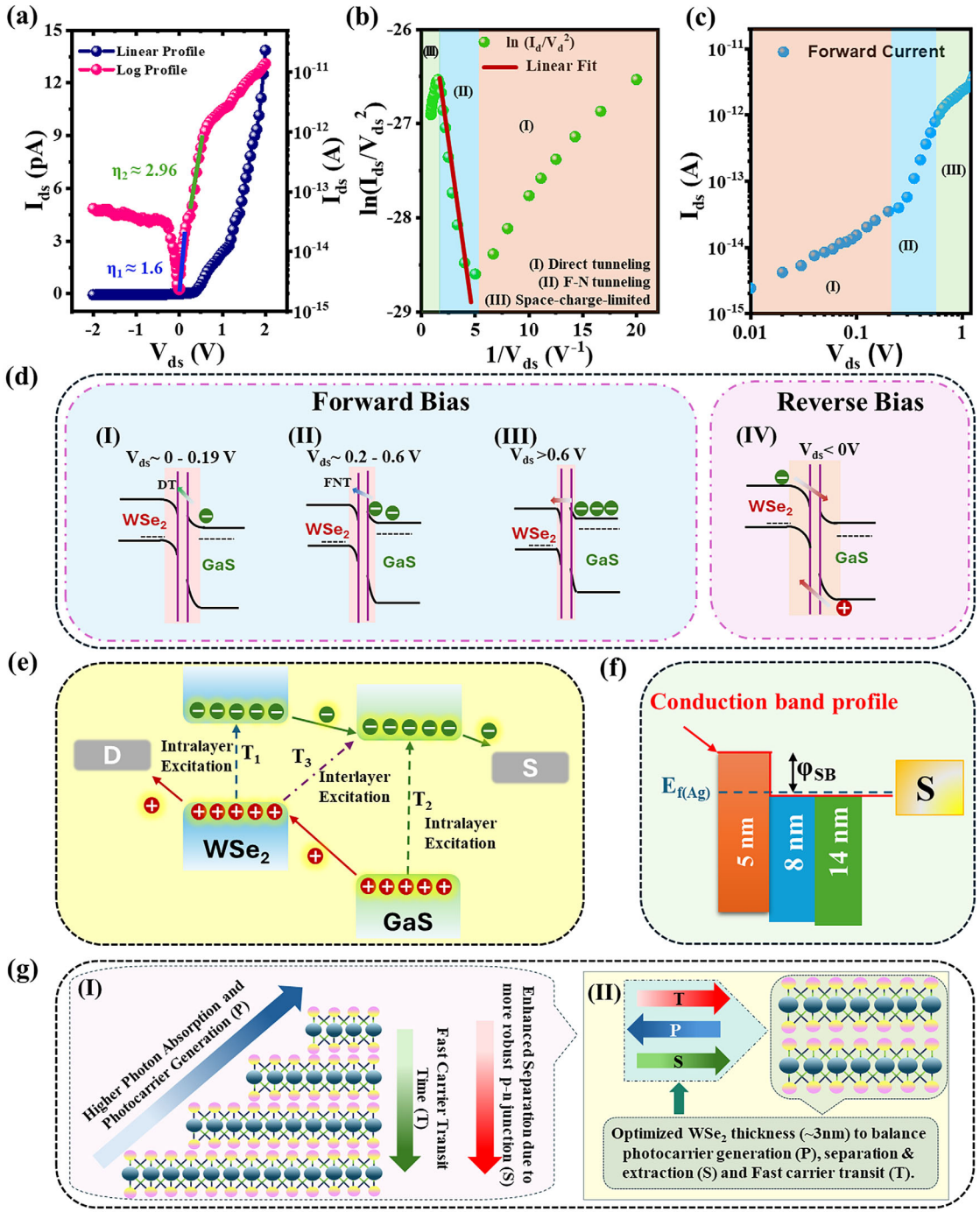

Figure 3. a) Dark I_d–V_d profile of the photodiode, showing two distinct linear regions with ideality factor η_1 and η_2 of 1.6 and 2.96, respectively. b) ln (I_d/V_d^2) versus $1/V_d$ plot of the diode forward current regime, showing three distinct operation regions (DT, FN, and SPLC). c) Double log I_d–V_d plot of the forward current. d) Schematic illustration of transport characteristics of the photodiode under forward and reverse bias conditions. e) Pseudoband potential of the heterojunction under quasiequilibrium state of illumination, illustrating intralayer transitions (T_1 and T_2) and interlayer transition (T_3). f) Proposed layer-dependent evolution of conduction band profile of GaS with respect to silver contact. g) Strategy for optimization of WSe_2 layers for efficient charge generation, separation, and extraction.

the GaS side was connected to ground. A clear rectifying characteristic of a conventional p–n junction is observed in Figure 3a with a rectification ratio of over 10^2. Interestingly, the log-scale plot of the drain current reveals two distinct linear regions in the forward bias configuration: 0.01 V < V_{ds} < 0.19 V, with a diode ideality factor (η) of ≈1.6 and 0.2 < V_{ds} < 0.6 V, with an ideality factor of ≈2.96, in accordance with the Shockley diode equation. To understand the tunneling phenomenon, the forward current I_d–V_d characteristics was replotted, as shown in Figure 3b, with three distinct regions. A low-voltage DT regime is observed under low bias configuration (region (I)), and an FN tunneling regime (region (II)) with negative slope which could be expressed by the following expression[30,31]

$$I_d \propto \begin{cases} V_d e^{\left(-\frac{2d\sqrt{2m^*\phi_T}}{\hbar}\right)} & \left(V_d < V_{FNT}\right) : \text{DT} \\ {V_d}^2 e^{\left(-\frac{4d\sqrt{2m^*{\phi_T}^3}}{3\hbar eV}\right)} & \left(V_d > V_{FNT}\right) : \text{FNT} \end{cases} \quad (1)$$

where m^* is the electron effective mass, ħ is the reduced Planck constant, d is the barrier thickness, and Φ_T is the tunneling barrier height. The tunneling threshold voltage, a V_{FNT} of ≈0.195 V, could be obtained from Figure 3b and tunneling barrier Φ_T could be estimated from this threshold to be roughly 0.195 eV ($V_{FNT} = \Phi_T/e$). Upon further investigation, using a double log plot of the I_d–V_d characteristics, as shown in Figure 3c, one could notice that the DT region shows a linear regime portraying an approximate Ohmic behavior, as expected in the case of DT effect in region (I), due to thermionic emission. The formation of band bending of the device under applied potential is illustrated in Figure 3d. The barrier hindering the charge carrier is trapezoidal in this region as illustrated in Figure 3d, region (I). Furthermore, the current is found to increase more rapidly in region (II) at a higher applied drain–source potential; the barrier tends to form a triangular shape and becomes narrower, leading to FN tunneling (Figure 3d, region (II)). At much higher voltage (V_d > 0.6), the current is limited by the SPLC (Figure 3d region (III)).[32] The device shows a rectification ratio of ≈250, which could be further enhanced by forming asymmetric accumulation type contacts at both ends (i.e., a higher work function contact at the WSe_2 end and lower work function contacts at GaS).

We then examine the charge transport and excitonic transfer in our vdW heterojunction as outlined in the pseudoband diagram in Figure 3e. During quasiequilibrium state of illumination, at lower wavelengths (<450 nm), the intralayer excitation T_2 dominates the excitonic dissociation in GaS layer producing electron–hole pairs that are separated by the built-in potential in the heterojunction, causing electron and hole transit toward the source and drain contacts, respectively. As the excitation wavelength transitions toward higher wavelength, contribution of excitonic transitions from WSe_2 with intralayer excitation T_1 aids to the photocurrent generation with highest responsivity observed at 450 nm and maximum open-circuit voltage before saturation (discussed later) with the peak photovoltaic responsivity of the device observed (Figure S9c, Supporting Information) at this wavelength. At illumination wavelengths below the bandgap of GaS (i.e., λ > 490 nm), intralayer excitation T_1 path dominates excitonic transitions and the responsivity of the device starts to decay (Figure S9c, Supporting Information), with only the ultrathin WSe_2 absorber layer facilitating in the excitonic dissociation mechanism. This is further supported by the report,[7] where GaS photoconductors demonstrated negligible photoresponse beyond 470 nm. As the illumination reaches beyond bandgap of ultrathinWSe_2, (λ > 850 nm), the photovoltaic photoresponsivity for the device demonstrated a pronounced depression (Figure S9c, Supporting Information), consistent with a significant decrease in the absorption characteristics of WSe_2[33] and interlayer excitonic transition T_3 likely plays a significant role in the charge transport and excitonic dissociation, as evidenced from the difference in responses observed among 810, 980, and 1064 nm illuminations (discussed later). Moreover, local photocurrent line scan measurements under photovoltaic mode (Figure S18, Supporting Information) reveal the photocurrent originates from the heterojunction region of the detector.

We subsequently examine the significance of the optimized thickness of the GaS and WSe_2 layers in our investigated devices. In our investigation of multilayered GaS on h-BN, Ag/Au vdW contacts demonstrated the least deviation from linearity in the low bias regime (±500 mV) for a thickness above 8–10 nm. Any thickness lower than the mentioned value would significantly deviate the linearity, signifying the emergence of a Schottky barrier (details in Section S5 in the Supporting Information). A plausible explanation of this trend could be explained as thickness decreases, bandgap starts widening with decrease in free-carrier concentration and available density of states, shifting the conduction band edge to lower energy values, away from the Fermi level of the contact as outlined in Figure 3f. Additionally, the thickness of the WSe_2 layer plays a crucial role in determining the robustness of the p–n junction. Earlier, it was reported that a thicker WSe_2 would shift the work function to lower energy levels, promoting an n-type transition,[34] supporting our KPFM findings as well (details in Section S9 and Figure S7 in the Supporting Information). This could explain the reason for reduced performance, in device-2, which is comprised of a thicker WSe_2 region, and the optoelectronic characteristics and KPFM results suggested that the built-in potential developed in junction region may have degraded (SPD ≈ 125 mV), undermining its optoelectronic performance (discussed later). This may be one of the probable factors. Additionally, another important contributing factor could be the optimized thickness of WSe_2 layer (3 nm), which may play an important role in charge-carrier separation and extraction. It is well established that monolayer TMDC exhibits an absorption of only 5% of the incident illumination. As the thickness of WSe_2 increases to a few layers, the absorption should correspondingly increase, thereby promoting higher photocarrier generation (P), as illustrated in Figure 3g-I (blue arrow). However, a scaling limit is reached due to a trade-off between photocarrier generation in multiple layers (P) and the efficiency of their separation and extraction (S). This limitation arises from the intralayer recombination, which tends to dominate over the extraction and separation mechanism (red arrow in Figure 3g-I), specially when thicker WSe_2 is used in the heterojunction, and a degradation in the robustness of the p–n junction is expected, as stated earlier. Moreover, a reduced thickness of the photosensitive layer is expected to facilitate faster transit of photocarriers (T), as illustrated in Figure 3g-I (green arrow), thereby decreasing the

likelihood of higher recombination losses. Consequently, achieving optimal device performance necessitates a balance between photocarrier generation, recombination, and transit, as depicted in Figure 3g-II. This balance appears to be achieved in device-1 and could serve as a key factor for reduced performance observed in device-2.

Moreover, a device with thicker GaS (≈13.2 nm) and an ultrathin WSe_2 of 3.8 nm (device-3) was also investigated and was found to have lower power conversion efficiency (PCE) than device-1, despite having a larger SPD, indicating poor charge separation and extraction characteristics as well. The measured SPD from KPFM was higher (≈216 mV) likely due to a thicker GaS region with ultrathin WSe_2, similar to device-1, suggesting a robust p–n junction. However, observation of lower PCE could be explained using Figure S6e,f (Supporting Information). As illustrated, when the GaS thickness (t_1) as in device-1 (Figure S6e, Supporting Information) is lower than that of (t_2) as in device-3 (Figure S6f, Supporting Information), the contact region for charge-carrier extraction is positioned closer to the depletion region of the junction in the vertical direction. Consequently, the carrier transit path (L_1) in device-1 is shorter than the transit path (L_2) in the thicker GaS region of device-3. This configuration significantly reduces the photocarrier recombination likelihood and enhances carrier extraction efficiency in device-1, which demonstrates a PCE of 0.8%, compared to the 0.4% PCE observed in device-3 with the thicker GaS region at 405 nm (more comparative analysis presented later).

For high-performance device operation of vdW optoelectronics, it is generally expected that metal–vdW-m junction is free of Schottky barrier and forms Ohmic contact that sponsors ultralow contact resistance. The emergence of Schottky barrier in metal–vdWm junction is strongly correlated to the metal–vdWm interfacial interactions that trigger FPL, similar to the case observed in metal–3D semiconductor FLP characteristics, despite having near perfect surface states, due to absence of surface dangling bonds. The origin of FLP in metal–vdW-m interface has been thoroughly investigated,[11–13] and the cause has been identified to be from the formation of a large number of defect states that occur when metal is directly deposited on the surface of the vdW-m (more discussion in Section S6 in the Supporting Information). This diminishes the prospect of achieving Ohmic contact, despite using metals with matching work functions, as the metal work function is pinned to the midgap states of the vdW-m. This is very significant for a vdW-m with a considerably large bandgap like GaS, for which self-powered optoelectronic devices may not have been possible till date. Additionally, the defect-induced gap states are also hotspots for scattering, recombination, and trapping of photogenerated carriers. This negatively impacts key figure of merits of photodetectors, especially reduced efficiency, linear dynamic range, and sluggish response times. Moreover, the dark current of the device is affected in two ways: i) the dark current is significantly increased due to injection of thermalized carriers from the midgap states and ii) the formation of hybrid bonds between the metal and vdW-m leads to loss of vdW gap between the metal–vdW-m junction, further escalating the flow of dark current. The effect is more pronounced for few-layer vdW-m when the metal pierce through the top layer and create bonds with the subsequent layers underneath as well, reducing the effective resistance for dark current path (Section S6 and Figure S5a(iii), Supporting Information). As a result, the overall performance of the photodetector is greatly reduced (as is observed in the case of device-4). On the contrary, using a vdW transfer metal contact (as for the cases of devices-1–3) significantly reduces FLP,[11] since the transfer metal method does not introduce any perforations/damage/defects in the vdW-m and promotes a pristine interface (Figure S5b, Supporting Information). The intrinsic defects within the vdW-m are the only source of FLP to transfer metal contact, which is negligible compared to defects induced by EBL-induced perforations in device-4. Consequently, the transfer metal method helps in efficient alignment of work-function-based metal–Schottky barrier engineering for efficient photocarrier extraction, pristine metal–vdW-m interface eliminating the gap state induced scattering, recombination, and trapping of photocarriers, enhancing the overall performance of the detectors.

Additionally, we looked at the role of the structure of the device in enhancing the device's performance. Previous reports of GaS-based photodetector structures[3,7–9] employed a lateral configuration. Since GaS has a large bandgap of ≈2.5 eV, it is expected to have low charge-carrier mobility due to reduced free charge-carrier concentration. Hence a lateral heterojunction with an extended GaS layer before the contact would introduce unnecessary increment in the charge-transport path, (more details in Section S8 in the Supporting Information). This additional path increases photocarrier recombination losses due to longer transit time and increased series resistance, ultimately lowering charge collection efficiency. Overall, a synergistically optimized effect of efficient charge-carrier generation, separation, and extraction takes place in this optimized heterojunction based on the precisely adjusted thickness of GaS–WSe_2, integration of vdW metal contacts (vdW–MC) along with the device structure.

A robust heterojunction photodiode showing fast response and broadband characteristics should be a synergistically engineered device so that it balances maximum photocarrier generation, enhances the charge separation and provides an efficient route for charge carrier extraction, under illuminated conditions. **Figure** 4a represents the output curve of the device with increasing light power P_{in} from 0.067 pW to 14.44 nW at 450 nm illumination. As the light power increases, a significant increase in the short-circuit current (I_{SC}) and open-circuit voltage (V_{OC}) is observed, which can be further substantiated from the zoomed linear scale plot of I_d–V_d in Figure 4b, clearly stating the crossover at the respective axis. The photovoltaic effect of our optimized heterojunction was assessed using the measurements of I_{SC} and V_{OC}, (Figure 4c). V_{OC} shows a linear scaling dependence with the log of the input power density (PD_{in}), with gradual evident saturation as PD_{in} reaches ≈50 mW cm^{-2}, with a maximum V_{OC} of 0.36 V. The photocurrent (I_{ph}) of the detector is defined as the difference between drain current under illumination and dark condition ($I_{ph} = I_{light} - I_{dark}$). In the case of our a-vdW photovoltaic detectors, where there is absence of source–drain bias, the dark current (I_{dark}) of our investigated devices were in the ≈*fA* range, which is impressively low and the current under illumination (I_{light}) could be written as $I_{light} \approx I_{SC}$. Interestingly, the double log plot of I_{SC} versus PD_{in}, shows an impressive linearity, with no saturation observed in our investigated maximum PD_{in} (52.7 mW cm^{-2}), with an impressive power exponent, α (i.e., $I_{SC} \propto PD_{in}^{\alpha}$) of

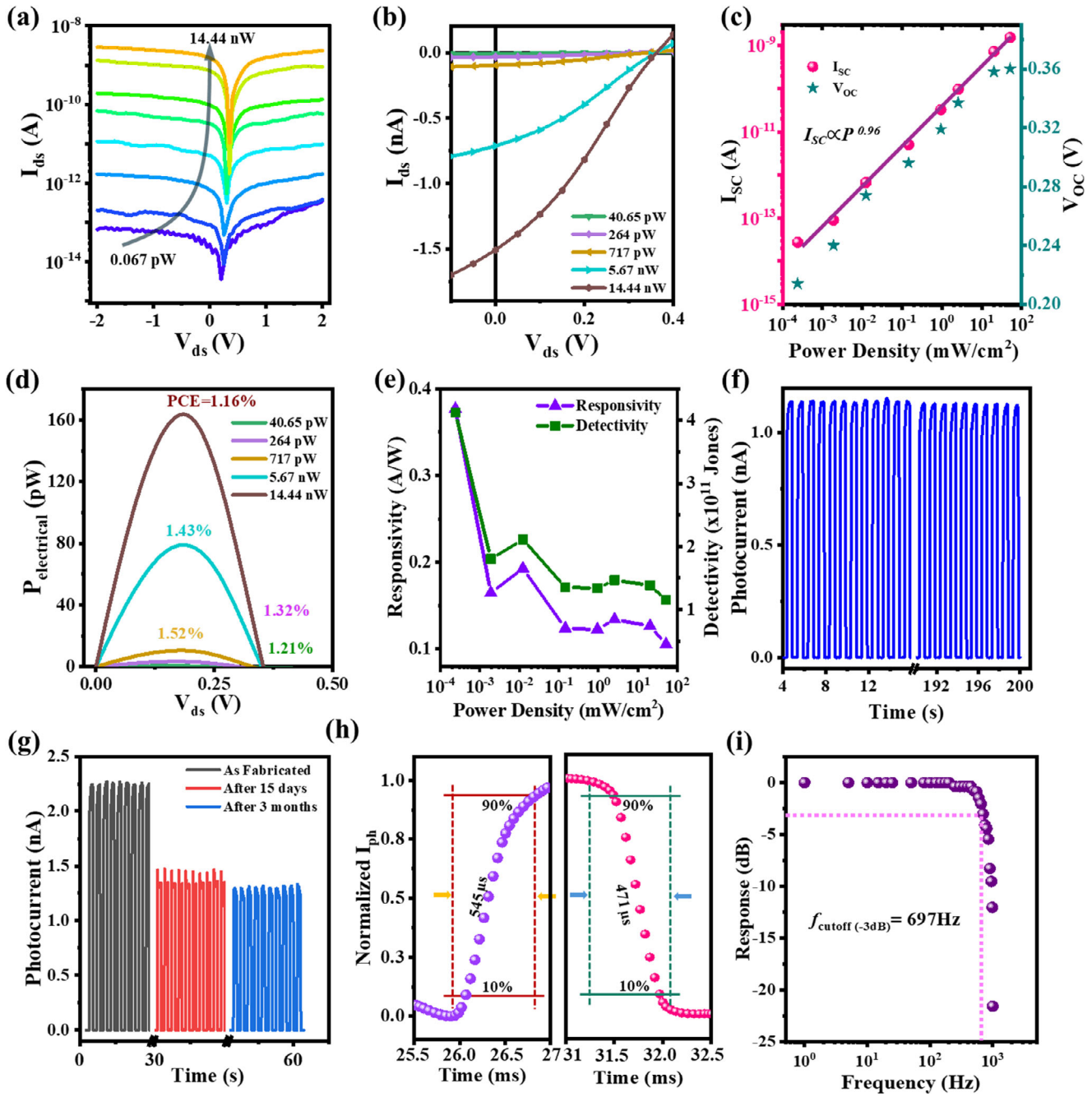

Figure 4. Optoelectronic characteristics of the device under 450 nm illumination. a) Evolution of log I_d–V_d characteristics under increased illumination power. b) Zoomed region of I_d–V_d showing clear I_{SC} and V_{OC}. c) I_{SC} and V_{OC} versus power density plot showing a linear region for I_{SC} and no saturation with an LDR of 106.7 dB and V_{OC} saturation at 0.36 V. d) Electrical power characteristics of the photodiode under increased illumination showing various PCE under varied illumination conditions. e) Responsivity and detectivity versus power density of the device, showing a peak photovoltaic responsivity of 376.76 mA W^{-1} and a detectivity of 4.12 × 10^{11} Jones. Temporal photocurrent response of the device at 405 nm illumination, showing f) 200 cycles of switching stability with no degradation, g) evolution of stability of the device under a course of 90 days observation period, h) rise and fall times of the device showing 545 µs (rise) and 471 µs (fall) edges, and i) frequency response showing a cutoff (−3 dB) at 697 Hz.

0.96. The linear regime of the I_{SC}–PD_{in}, can be quantified by an important figure of merit, the LDR of the photodiode, in dB, and could be obtained using

$$LDR = 20\log\left(PD_{in(max)}/PD_{in(min)}\right) \quad (2)$$

where, $PD_{in(max)}$[$PD_{in(min)}$] is the maximum (minimum) PD_{in} of the linear region. Based on the reported results in Figure 4c, the LDR of our optimized junction is 106.78 dB. It is worth noting that 106.7 dB is still underestimated due to the limited illumination conditions available at our disposal. Our reported V_{OC}

of 0.36 V, an LDR of 106.78 dB, and ultralow dark currents of ≈*fA* in this work are among the most impressive ones in single vdW heterojunctions and even exceeds that of more recently investigated double heterojunctions under similar illumination conditions.[35] This suggests GaS–WSe_2 vdW heterojunction for similar applications would be an excellent alternative.

Owing to the impressive power exponent value of 0.96 and a large V_{OC} of 0.36, we further investigate the ongoing photocarrier generation and recombination mechanisms in our synergistically engineered heterojunction photodiode. For vdW interfaces, two primary physical phenomena are involved in the interlayer recombination mechanisms:[36,37]

1) *Shockley–Read–Hall (SRH) Recombination*: This process is driven by the inelastic tunneling of majority carriers into trap states, often referred to as monomolecular recombination.
2) *Langevin Recombination*: This occurs due to Coulomb interactions, where electron–hole pairs recombine at the junction shortly after their creation, also known as bimolecular recombination.

In the heterojunction region, one of these mechanisms may dominate, although both can occur simultaneously. To quantitatively elucidate the recombination process, the following equation can be used[38]

$$\frac{dV_{OC}}{d\ln\left(PD_{in}\right)} = \frac{2}{\beta}.\frac{K_B T}{q} \tag{3}$$

where β represents the recombination order (1: SRH recombination and 2: Langevin recombination). K_B is Boltzmann's constant, T is the temperature, and q is the unit charge. From the fitting of the experimental data, we obtain β to be 1.84, suggesting the synergistic optimized device is dominated by Langevin recombination. This is very significant as upon synergistic engineering, the device tends to suppress/reduce trap-mediated recombination, when compared to device-2 and device-3, with more discussion presented later. The reason could be further related to the thickness of the optimized layers of both GaS and WSe_2 for robust p–n junction, shorter carrier transit path for GaS layer to reduce trap-assisted recombination, ultimately benefiting the device for efficient charge separation and extraction.

Additionally, we also investigated the electrical power production from the diode ($P_{el}/I_{ds}.V_{ds}$) with a maximum power produced as 0.162 nW (Figure 4d) and demonstrates a much larger electrical power production capacity than GaSe–MoS_2[39] heterojunction under similar illumination conditions. The calculated PCE using the maximum electrical power $P_{el_{max}}$ (i.e., PCE = $P_{el_{max}}/P_{in}$) for the same P_{in}, is represented in Figure 4d. With an increase in P_{in}, the PCE also increases to a maximum value of 1.52%, before slight reduction at a maximum investigated P_{in} of 14.44 nW, demonstrating a gradual saturation of its capacity of energy conversion and light harvesting at the p–n junction, likely due to the saturation of the photovoltage developed at the junction. Our reported PCE in this work is significantly larger than WSe_2–Bi_2O_2Se heterojunction (0.428%)[22] in the similar thickness regime, suggesting its applicability in energy-harvesting applications as well.

The photovoltaic responsivity (R) of the device was obtained using the ratio of the photocurrent to the input optical power (i.e., $R = I_{ph}/P_{in}$). As represented in Figure 4e, a maximum photovoltaic responsivity of 376.76 mA W^{-1} was obtained, comparable to single junction InSe–Gr a-vdW device[40] and larger than recently investigated $PdSe_2$–$MoTe_2$ heterojunctions.[41] Along with responsivity, external quantum efficiency (EQE) is an important bench marking parameter for photovoltaic type devices and could be estimated based on the responsivity of the device and illumination wavelength (i.e., EQE = $R.h.c/e.\lambda$). The estimated EQE of the photodiode at various wavelengths under self-biased condition is illustrated in Figure S9a (Supporting Information). The device shows an excellent EQE evolution, maintaining a value of ≈30% at high illumination intensity in the 400–450 nm region, suggesting excellent photovoltaic performance for solar cell applications as well.[42] Moreover, for competitive performance comparison, the fill factor (FF) of our device was also obtained. FF is a measure of solar cell quality, indicating how closely the actual maximum output power follows the theoretical maximum value for the device and could be obtained as FF = $P_{el_{max}}/I_{SC}.V_{OC}$. The polychromatic FF of our device has been presented in Figure S9b (Supporting Information) with varied illumination intensity. Our device exhibits an excellent value of FF within 0.28–0.35 even at higher power density, suggesting the device is indeed a contender for power harvesting in the solar spectrum region, and potentially contributes to harvesting the 4% UV solar irradiance, which is otherwise overlooked in conventional silicon solar cells.

Another important figure of merit for photodetectors is the specific detectivity, D^* of the device, which can be derived from noise equivalent power (NEP) of the photodetector using the following equation: $D^* = \sqrt{A}/\text{NEP}$, where A is the device active area. The inference of noise currents in photodetectors could be made from the summation of Johnson noise, shot noise, and flicker noise. The shot noise current (i_{SN}) in a photodiode could be estimated from the following equation using the dark current: $i_{SN} = \sqrt{2.q.I_{dark}}$, where I_{dark} represents the dark current of the device. Additionally, the flicker noise current could be extracted from the *1/f* fitting at the low frequency region of the noise power density plot. An estimation of the D^* could be readily obtained from the following equation, $D^* = (R_\lambda.A^{1/2})/(2.q.I_{dark})^{1/2}$, R_λ is the wavelength-specific responsivity and q is the unit electron charge. The maximum estimated detectivity from the abovementioned equation at 450 nm illumination could be obtained as 7.32×10^{12} Jones. However, the above-mentioned estimation is valid when the dominant noise factor in the device is the shot noise and is a crucial aspect at high frequencies and could be overestimated by several orders of magnitude, compared to noise contribution from flicker noise at low frequencies. To further evaluate the discrepancies, we investigate the presence of flicker noise from the noise power density plot (details in Section S10 in the Supporting Information). The noise power density plot reveals presence of sub-log-linear fitting of $(1/f)^\alpha$, suggesting contribution of flicker noise presence. The noise current obtained from linear fitting of the noise density plot could be used for estimating the NEP using the equation: NEP = i_{fN}/R, where i_{fN} is the flicker noise current and R is the responsivity the device. The obtained NEP is 1.28 fW $Hz^{-1/2}$, which could be used to obtain a maximum D^* value of 4.12×10^{11} Jones, as outlined Figure 4e. This reveals that indeed

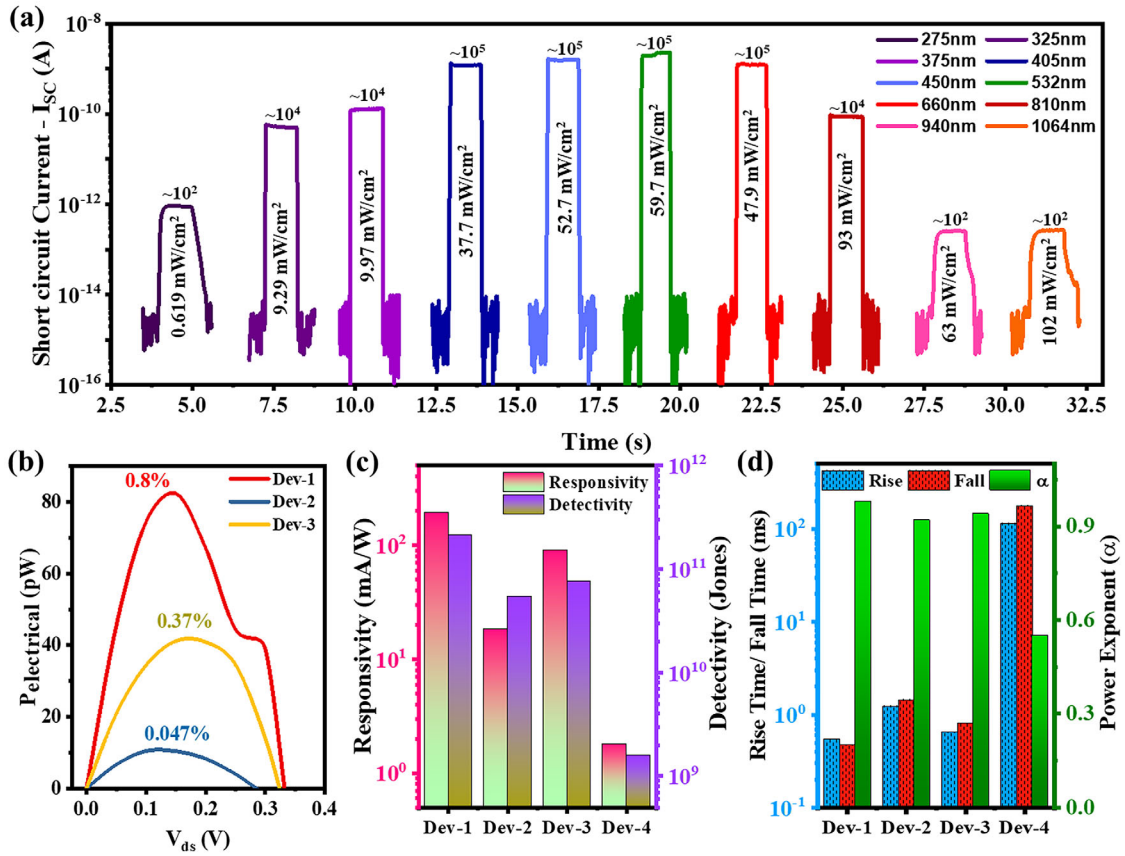

Figure 5. a) Photovoltaic temporal response of the device under maximum available illumination conditions of the device under various wavelengths. The device shows a photovoltaic response between 275 and 1064 nm, with a peak on–off ratio of 10^5. b) Evolution of PCE of the fabricated a-vdW devices, suggesting the need for synergistic thickness engineering for efficient light-harvesting characteristics, with a maximum PCE for synergistically optimized device-1 and minimum for device-2 having a thicker GaS and WSe_2 regions, with intermediate performance from device-3, constructed from ultrathin WSe_2, similar to device-1 and slightly thicker GaS than device-1. c) Comparison of responsivity and detectivity for the fabricated devices under similar illumination conditions at 405 nm. d) Comparison of rise/fall time and power exponent of all the fabricated devices under 405 nm illumination.

estimation of the presence of dominant shot noise would lead to an underestimation of the detectivity of the device. Henceforth, we report the detectivity of our findings based on NEP.

We next look into the temporal photocurrent response of the device. The photovoltaic response speed is an essential performance parameter for a self-powered photodetector, as it measures how promptly the device responds to rapidly changing incident light. This characteristic is particularly important for applications that demand quick detection and adaptation to fluctuating light conditions. Owing to the presence of the strong built-in potential from the type-II heterojunction, the device is expected to have a fast response. Figure 4f represents the time-resolved photocurrent of the device at 1 Hz with 405 nm illumination, with 200 switching cycles. A stable photoswitching is observed over 200 cycles with no evident degradation in the device's photocurrent, suggesting a robust performance. Furthermore, to evaluate the stability of the device under ambient storage, time-resolved photocurrent measurements were repeated over a period of 3 months as represented in Figure 4g and a slight reduction in the photocurrent of the device was observed from day 1 to day 15 with no significant noticeable changes in the photocurrent afterward, suggesting superior stability of the device (more discussion in Section S7 in the Supporting Information). The consistent and reproducible photo response after 200 switching cycles along with long-term stability of the device demonstrates the exceptional reliability of the self-powered photodetector. The rise time and decay time of the device were obtained between 10% and 90% of the maximum I_{ph}, as illustrated in Figure 4h, where a rise time (fall time) of 545 µs (471 µs) was observed, demonstrating superior photovoltaic response speeds compared to multilayer graphene (MLG)/$ReSe_2$/$SnSe_2$ (752/928 µs),[30] GaSe–MoS_2 (5 ms/5 ms),[39] GaSe–$MoSe_2$ (16 ms/16 ms),[43] and $PdSe_2$–$MoTe_2$ (3.5 ms/3.7 ms)[41] heterojunction-based devices. Additionally, a series of measurements conducted at multiple laser modulation frequencies (Figure 4i) display that the 3 dB bandwidth (f_{3dB}) of the optimized photodiode is 697 Hz, which is in good agreement with the measured photo response time. These results indicate the proposed device's capacity to monitor rapid optical signals and its great potential for high-speed photodetection.

Furthermore, we also investigated the on/off ratio of the device under various wavelengths at maximum illumination intensity at our disposal, as illustrated in **Figure 5a**, in a self-powered configuration. The device demonstrated an excellent

broadband photovoltaic response ranging from 275 to 1064 nm, achieving a peak on/off ratio of ≈10^5 from 405 to 660 nm, comparable to WSe_2–Bi_2O_2Se[22] and Bi_2O_2Se/In_2S_3[31] heterojunctions. Additionally, interlayer transitions were evident from the weaker temporal responses, with an on/off ratio of 10^2 observed for 940 and 1064 nm illumination. The wavelength-dependent peak responsivity and detectivity of the device are illustrated in Figure S9c (Supporting Information), highlighting its exemplary photovoltaic performance. It is important to note that the detection bandwidth was limited by the available light sources during this investigation and may not represent the maximum bandwidth-limited response of the device. We also examined the wavelength-dependent transition of the power exponent, α, as depicted in Figure S9d (Supporting Information). In conventional photodiodes, the power function α, derived from the double logarithmic plot of I_{SC}–PD_{in} serves as a measure of the device's charge extraction performance figure of merit, with a theoretical maximum value of 1. However, in practical applications, the value of α typically falls below 1, indicating the presence of recombination processes occurring in trap states.[44] This reduction in α reflects the inefficiencies in charge extraction due to these recombination pathways, which can adversely affect the overall performance of the photodiode. Notably, at lower wavelengths (<375 nm), α was less than 0.9. As the wavelength is increased to 405 nm, α increases to 0.98, maintaining values above 0.95 between 405 and 810 nm, and approaching near unity (0.99) at 940 nm (Figure S9d,e, Supporting Information). These findings suggest that some trapping and recombination occur at lower wavelengths, likely due to interaction with atmospheric absorbates which serve as charge trapping/detrapping centers under UV illumination,[45] while negligible trapping is observed as the wavelength increases, indicating superior trapping/recombination-free performance in the near-infrared (NIR) region. The reported linearity across a wide range of wavelengths is among the highest for single-junction photodiodes[37,41] and is comparable to recently reported dual floating junction detectors.[46]

Interestingly, all the investigated a-vdW devices (devices-1–3) exhibited a power exponent (α) greater than 0.9, with values of 0.98 for device-1, 0.92 for device-2, and 0.94 for device-3. In contrast, an EBL-patterned control device (device-4) demonstrated a significantly lower α of 0.55. Given that all devices were fabricated under identical conditions and have similar structure and active area, the inferior performance of device-4, patterned using traditional contact integration methods, suggests EBL patterned devices may have undergone significant interface modifications in the contact region, likely due to e-beam-induced damages in the contact region and/or metal impingement induced trap states,[14] inevitably making the device susceptible to increased FLP and charge trapping in the contact region. Additionally, device-4 presented no rectification and drain-voltage-induced conduction characteristics between the applied drain voltage of ±2 V, under dark conditions, suggesting emergence of large Schottky barrier at the contact regions. The persistent dark current in the device was an order of magnitude higher than the a-vdW devices, suggesting injection of random thermalized carriers from the midgap states as stated earlier. This finding is particularly relevant for GaS-based heterojunctions due to GaS's larger bandgap and more likeliness of being affected by FLP-induced Schottky barrier and degrading performance, as evidenced from device-4. The lower values of α for devices-2 and 3 could be attributed to interlayer recombination centers, rather than contact-induced degradation and charge trapping, further emphasizing the need for a synergistic approach to thickness engineering for improved performance, as demonstrated by device-1. To substantiate our claim, we compare the recombination order value (β) for the three a-vdW devices at 405 nm, obtained using Equation (3). The results show that β for device-1 is 1.62, indicating dominant Langevin recombination. In contrast, device-2 and device-3 exhibited β values of 1.2, and 1.3, respectively, both suggesting dominant SRH recombination occurring in trap states due to defects in the semiconductor. This analysis reinforces our assertion regarding the necessity of a robust p–n heterojunction and thickness-optimized layers. Such optimization ensures that when photocarriers are generated, they are swept apart by the strong built-in potential before being trapped in defect states. Furthermore, our findings suggest that through meticulous optimization in vdW devices, we can achieve a scenario where dominant Langevin recombination persists. This may represent the ultimate performance limit in the proposed device structure due to low charge-carrier mobility[47] of GaS, highlighting the performance limit of efficient charge extraction mechanisms observed in device-1.

A comparison of the PCE of the a-vdW devices at 405 nm further supports this claim, as shown in Figure 5b. Device-1 achieved the highest PCE of 0.8%, while device-3 exhibited half the PCE of device-1 at 0.37%, despite having a slightly higher SPD, and device-2 illustrated a PCE that was one order of magnitude lower than device-3, at just 0.047%, under similar illumination conditions. Additionally, a stark difference is observed between other figure of merits such as responsivity, specific detectivity and rise/fall time as illustrated in Figure 5b,c, for a-vdW devices and EBL-patterned device as well, with device-1 outperforming the other three devices. These findings further indicate that device-1 possesses the most synergistically optimized conditions in terms of thickness and structure for a robust rectifying p–n heterojunction, capable of efficient photocarrier generation, separation, and extraction, while the vdW-MC ensures a pristine interface, free of FLP further aiding to efficient charge carrier extraction and superior photodetection.

To further explore the device's versatility for multifunctional applications, we investigated its gate tunable characteristics. As illustrated in Figure S9f (Supporting Information), the device exhibits a strong ambipolar gate tunable characteristics under various applied V_{ds}. We also assessed the device's responsivity under gate tunable conditions (Figure S9g, Supporting Information), demonstrating a gate tunable ambipolar responsivity of greater than 10^5 A W^{-1} at a gate voltage (V_g) of ±40 V. This implies that the device can be tuned for high photoresponsivity applications as well.

2.3. Potential Application in Multifunctional Optoelectronics

To evaluate the device's potential as an image sensor, device-1 was incorporated into a single-pixel imaging system, as depicted in **Figure 6a**. In practical applications, image sensing is typically conducted using sensor arrays integrated with readout circuitry

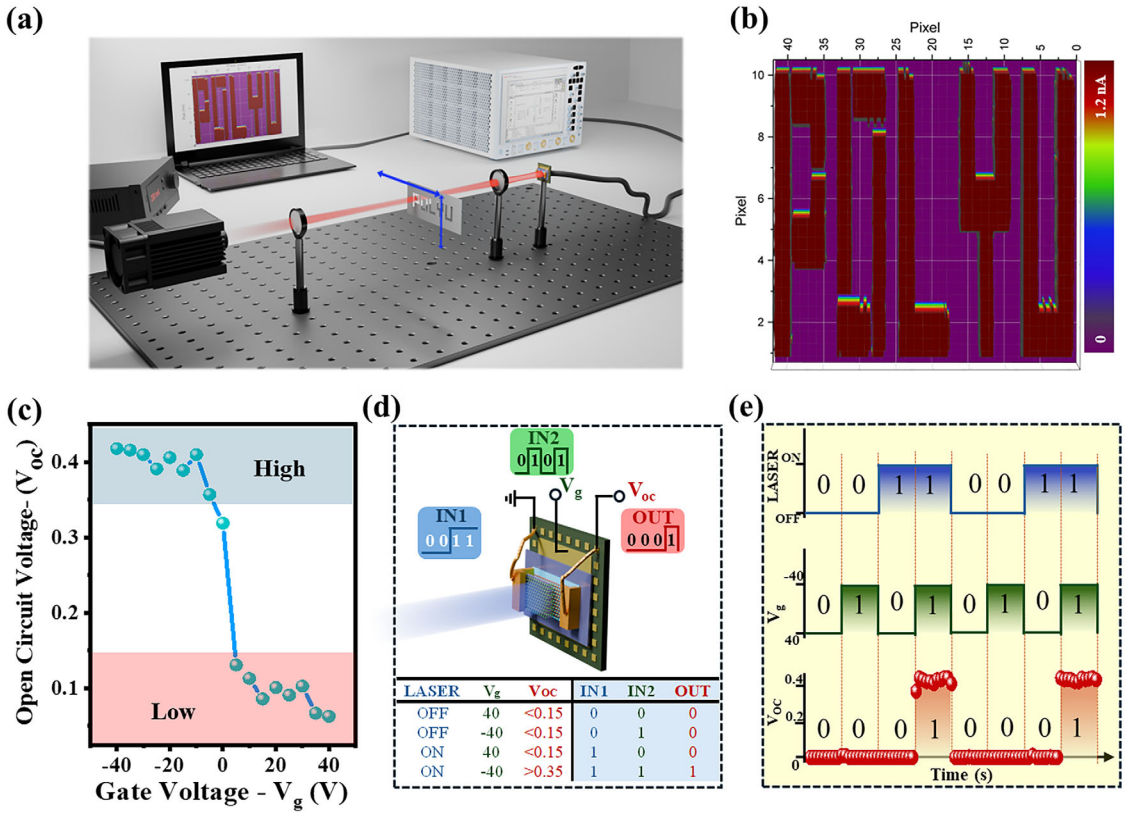

LASER	V_g	Voc	IN1	IN2	OUT
OFF	40	<0.15	0	0	0
OFF	-40	<0.15	0	1	0
ON	40	<0.15	1	0	0
ON	-40	>0.35	1	1	1

Figure 6. a) Schematic illustration of a single-pixel imaging system. b) Reconstructed image of the pattern "P O L Y U." c) Variation of V_{OC}, with tuned V_g, under illumination at 405 nm. A state of high (V_{OC} > 0.35 V) and low (V_{OC} < 0.15) could be outlined in the sky blue and pink regions, respectively. d) Schematic illustration of the optoelectronic logic AND gate (top) and its corresponding state table (bottom). e) State trace and corresponding logic function demonstration of the optoelectronic AND operation.

and amplifiers. The quality of the acquired images is influenced by the pixel size, which is determined by the dimensions of the detector array. In contrast, single-pixel imaging systems mimic the functionality of array detectors by utilizing a single device. Such systems are often employed in scientific demonstrations to illustrate the capabilities of fabricated devices for imaging applications. For our demonstration, a patterned aluminum mask displaying the letters "P O L Y U" was positioned between the light source and the detector. The mask was programmed to move stepwise in the *x*–*y* direction using a motorized 2D stage. Light passing through the mask was focused onto the detector via a lens, generating photocurrent signals. The recorded photocurrent data, along with corresponding positional information were reconstituted into a 3D plot using computer software, thereby representing the image acquired by the sensor. Figure 6b displays the image captured using a 405 nm light source, while Figure S10 (Supporting Information) illustrates the imaging capabilities with an 810 nm light source. Notably, the excellent polychromatic imaging capabilities of the demonstrated photodiode can be attributed to its remarkable linearity and synergistic engineering, further supporting its suitability for high-resolution imaging applications at various wavelengths.

Additionally, we investigated the device's capability to function in gate-tunable optoelectronic logic applications. As previously mentioned, the device exhibits excellent gate tunability, allowing us to evaluate the variation of V_{OC} in response to varying V_g. This relationship is depicted in Figure 6c, where a maximum V_{OC} of 0.41 V is observed at a gate voltage of −40 V. As V_g is increased, V_{OC} demonstrates a pronounced change between gate voltages −10 and 10 V, stabilizing below 0.15 V, with further increment of V_g to +40 V. Consequently, a high state of V_{OC} is defined as values greater than 0.35 V, while a low state corresponds to values below 0.15 V (as shown in Figure 6c). The device schematic for the optoelectronic AND gate is illustrated in Figure 6d, accompanied by a state table that outlines the input conditions (light and V_g) and the corresponding output conditions (V_{OC}). The device exhibits a clear input–output relationship characteristic of an AND gate, as depicted in Figure 6e. This demonstrates its potential functionality in optoelectronic logic operations, reinforcing the viability of the device for advanced multifunctional optoelectronics.

A summary of all key performance metrics of all the fabricated devices could be found in Table S1 (Supporting Information), while a comparison between our synergistically optimized a-vdW device and other photodetector devices reported with outstanding performance, is presented in Table S2 (Supporting Information). Additionally, Table S3 (Supporting Information) represents a comparison of our device's performance with some high-performance 2D solar cells.

3. Conclusion

In summary, we have synergistically engineered a-vdW type-II heterostructure photodiode, leveraging a GaS–WSe_2 heterojunction, meticulously engineered to achieve favorable balance among photocarrier generation recombination, separation, transport, and extraction, eventually facilitating a highly sensitive, broadband photodetector. The device exhibits ultralow light detection capabilities with polychromatic unity approaching linearity, a photovoltaic responsivity and a detectivity of 376.78 mA W^{-1} and 4.12×10^{11} Jones, respectively. The device also demonstrates a large on/off ratio of 10^5, a substantial LDR of 106.78 dB, a stabilized large EQE of 30%, and an FF and a V_{OC} of 0.33 and 0.36, respectively, with response speeds of 545/471 µs, showing excellent prospects in imaging and solar cell applications. Moreover, demonstration of gate tunable ambipolar responsivity of the photodiode, further expanded its applicability in gate tunable optoelectronic logic gate. Our systematic investigation on key performance indicators like power exponent and PCE for multiple devices reinstates the need for meticulous engineering of vdW heterointerfaces, particularly the effects of vdW-m thickness and contact integration strategies that severely influence characteristics performance of the devices. Our results presented in this work open an exciting route for future investigations that can be universally adopted to achieve photovoltaic heterojunctions with near unity linearity in other vdW-m with moderately large bandgaps.

4. Experimental Section

Fabrication and Characterization of GaS/WSe_2 Heterojunction Devices: Traditional scotch tape/polydimethylsiloxane (PDMS)-based micromechanical cleavage and aligned dry transfer technique were performed to obtain the van der Waals heterojunction. In short, scotch tape was used to exfoliate h-BN, GaS, and WSe_2 (HQ graphene) and transfer to PDMS. The correct thickness of the flakes was identified under a microscope using optical contrast and then transferred onto a previously ultrasonically cleaned (acetone (2 min), isopropyl alcohol (IPA) (3 min), and deionised (DI) water (3 min)] and plasma-treated (O_2 Plasma, 100 W, 5 min) 300 nm SiO_2/Si^{++}, sequentially by means of a homemade aligned transfer stage. The heterojunction was annealed under 50 sccm Ar flow at 180 °C for 1 h to increase coupling efficiency and ensure efficient charge transfer between the layers. Van der Waals metal contacts were fabricated and integrated using a similar technique as,[48] detailed in Section S1 (Supporting Information), for devices-1–3. For contact integration of device-4 conventional EBL was employed, where the device was spin-coated (4000 rpm, 25 s) with polymethyl methacrylate (PMMA) resist (950A4, MicoChem) and baked for 90 s at 180 °C, exposed to e-beam pattern and consequently developed using methyl isobutyl ketone (MIBK) / IPA (1:3) developer. Ag/Au contacts (38 nm/22 nm) were sequentially deposited and finally lift-off was carried out using acetone. To confirm the height profiles and surface potential differences of the heterojunctions, AFM (for height profile) and KPFM (alignment of Fermi level) was employed (Asylum MFP-3D). Raman and photoluminescence spectroscopic characterizations were conducted using Witec Raman, 300R. Micro UPS was conducted using Thermo Fisher Scientific Nexsa. Cross-sectional HR-STEM and HAADF STEM EdX were carried out using Spectra 300.

Electronic and Optoelectronic Characterization: The electronic characteristic measurements in ambient conditions under dark and global illumination were carried out in a Probestation (Lakeshore) synchronized with a Keysight B1500 semiconductor parameter analyzer, signal generator, oscilloscope and variable intensity LASER (405, 450, 532, 660, and 1064 nm) and light-emitting diodes (LEDs; 275, 325, 375, 810, and 940 nm) (Thorlabs), calibrated using power meter and sensor (PM100D, S120VC) (Thorlabs).

Supporting Information

Supporting Information is available from the Wiley Online Library or from the author.

Acknowledgements

This work was financially supported by the Photonic Research Institute (PRI), (Project No. 1-CD6V), Research Institute for Advanced Manufacturing (RIAM) (Project Nos. 1-CD8V and 1-CDK6), The Hong Kong Polytechnic University, Hong Kong, China and Science, Technology and Innovation Commission of Shenzhen Municipality (Project Nos. JCYJ20241202130542054 and JCYJ20210324141206017), The Hong Kong Polytechnic University Shenzhen Research Institute, Shenzhen, China.

Conflict of Interest

The authors declare no conflict of interest.

Data Availability Statement

The data that support the findings of this study are available from the corresponding author upon reasonable request.

Keywords

all van der Waals, broadband photodiode, Fermi-level pinning, GaS–WSe_2 heterostructure, photovoltaic, type-II heterojunction, van der Waals contact

Received: November 14, 2024
Revised: March 8, 2025
Published online: March 24, 2025

[1] L. Britnell, R. M. Ribeiro, A. Eckmann, R. Jalil, B. D. Belle, A. Mishchenko, Y.-J. Kim, R. V. Gorbachev, T. Georgiou, S. V. Morozov, A. N. Grigorenko, A. K. Geim, C. Casiraghi, A. H. Castro Neto, K. S. Novoselov, *Science* **2013**, *340*, 1311.
[2] J. Wong, D. Jariwala, G. Tagliabue, K. Tat, A. R. Davoyan, M. C. Sherrott, H. A. Atwater, *ACS Nano* **2017**, *11*, 7230.
[3] P. Hu, L. Wang, M. Yoon, J. Zhang, W. Feng, X. Wang, Z. Wen, J. C. Idrobo, Y. Miyamoto, D. B. Geohegan, K. Xiao, *Nano Lett.* **2013**, *13*, 1649.
[4] B. Chitara, A. Ya'Akobovitz, *Nanoscale* **2018**, *10*, 13022.
[5] F. D. V. Araujo, V. V. Oliveira, A. C. Gadelha, T. C. V. Carvalho, T. F. D. Fernandes, F. W. N. Silva, R. Longuinhos, J. Ribeiro-Soares, A. Jorio, A. G. Souza Filho, R. S. Alencar, B. C. Viana, *Nanotechnology* **2020**, *31*, 495702.
[6] V. Zólyomi, N. D. Drummond, V. I. Fal'Ko, *Phys. Rev. B* **2013**, *87*, 195403.
[7] Y. Lu, J. Chen, T. Chen, Y. Shu, R. J. Chang, Y. Sheng, V. Shautsova, N. Mkhize, P. Holdway, H. Bhaskaran, J. H. Warner, *Adv. Mater.* **2020**, *32*, 1906958.
[8] T. Chen, Y. Lu, Y. Sheng, Y. Shu, X. Li, R. J. Chang, H. Bhaskaran, J. H. Warner, *ACS Appl. Mater. Interfaces* **2019**, *11*, 48172.

[9] Y. Lu, T. Chen, N. Mkhize, R. J. Chang, Y. Sheng, P. Holdway, H. Bhaskaran, J. H. Warner, *ACS Nano* **2021**, *15*, 19570.
[10] X. Zhang, R. Li, Y. Yu, F. Dai, R. Jiang, J. Guo, W. Hu, Z. Ni, J. Lu, *Laser Photonics Rev.* **2024**, *18*, 2300936.
[11] Y. Liu, J. Guo, E. Zhu, L. Liao, S. J. Lee, M. Ding, I. Shakir, V. Gambin, Y. Huang, X. Duan, *Nature* **2018**, *557*, 696.
[12] X. Zhang, Z. Kang, L. Gao, B. Liu, H. Yu, Q. Liao, Z. Zhang, Y. Zhang, *Adv. Mater.* **2021**, *33*, 2104935.
[13] Y. Jung, M. S. Choi, A. Nipane, A. Borah, B. Kim, A. Zangiabadi, T. Taniguchi, K. Watanabe, W. J. Yoo, J. Hone, J. T. Teherani, *Nat. Electron.* **2019**, *2*, 187.
[14] W. Song, L. Kong, Q. Tao, Q. Liu, X. Yang, J. Li, H. Duan, X. Duan, L. Liao, Y. Liu, *Small* **2021**, *17*, 2101209.
[15] C. M. Went, J. Wong, P. R. Jahelka, M. Kelzenberg, S. Biswas, M. S. Hunt, A. Carbone, H. A. Atwater, *Sci. Adv.* **2019**, *5*, aax6061.
[16] X. Zhou, X. Hu, S. Zhou, H. Song, Q. Zhang, L. Pi, L. Li, H. Li, J. Lü, T. Zhai, *Adv. Mater.* **2018**, *30*, 1703286.
[17] Z. Bian, J. Miao, T. Zhang, H. Chen, Q. Zhu, J. Chai, F. Tian, S. Wu, Y. Xu, B. Yu, Y. Chai, Y. Zhao, *Small* **2023**, *19*, 2206791.
[18] S. Park, T. Schultz, D. Shin, N. Mutz, A. Aljarb, H. S. Kang, C. H. Lee, L. J. Li, X. Xu, V. Tung, E. J. W. List-Kratochvil, S. Blumstengel, P. Amsalem, N. Koch, *ACS Nano* **2021**, *15*, 14794.
[19] D. J. Late, B. Liu, H. S. S. R. Matte, C. N. R. Rao, V. P. Dravid, *Adv. Funct. Mater.* **2012**, *22*, 1894.
[20] H. S. Ra, M. H. Jeong, T. Yoon, S. Kim, Y. J. Song, J. S. Lee, *Adv. Sci.* **2020**, *7*, 2001475.
[21] C. Jastrzebski, K. Olkowska, D. J. Jastrzebski, M. Wierzbicki, W. Gebicki, S. Podsiadlo, *J. Phys.: Condens. Matter* **2019**, *31*, 075303.
[22] P. Luo, F. Wang, J. Qu, K. Liu, X. Hu, K. Liu, T. Zhai, *Adv. Funct. Mater.* **2021**, *31*, 2008351.
[23] B. Peng, G. Yu, X. Liu, B. Liu, X. Liang, L. Bi, L. Deng, T. C. Sum, K. P. Loh, *2D Mater.* **2016**, *3*, 025020.
[24] W. Zhao, Z. Ghorannevis, L. Chu, M. Toh, C. Kloc, P. H. Tan, G. Eda, *ACS Nano* **2013**, *7*, 791.
[25] P. Chen, T. L. Atallah, Z. Lin, P. Wang, S. J. Lee, J. Xu, Z. Huang, X. Duan, Y. Ping, Y. Huang, J. R. Caram, X. Duan, *Nature* **2021**, *599*, 404.
[26] S. Yang, Y. Li, X. Wang, N. Huo, J. B. Xia, S. S. Li, J. Li, *Nanoscale* **2014**, *6*, 2582.
[27] B. J. Carey, J. Z. Ou, R. M. Clark, K. J. Berean, A. Zavabeti, A. S. R. Chesman, S. P. Russo, D. W. M. Lau, Z. Q. Xu, Q. Bao, O. Kevehei, B. C. Gibson, M. D. Dickey, R. B. Kaner, T. Daeneke, K. Kalantar-Zadeh, *Nat. Commun.* **2017**, *8*, 14482.
[28] G. Iannaccone, F. Bonaccorso, L. Colombo, G. Fiori, *Nat. Nanotechnol.* **2018**, *13*, 183.
[29] P. Zhang, Y. S. Ang, A. L. Garner, Á. Valfells, J. W. Luginsland, L. K. Ang, *J. Appl. Phys.* **2021**, *129*, 100902.
[30] Y. Pan, T. Zheng, F. Gao, L. Qi, W. Gao, J. Zhang, L. Li, K. An, H. Gu, H. Chen, *Small* **2024**, *20*, 2311606.
[31] M. Chen, X. Chen, Z. Wu, Z. Huang, W. Gao, M. Yang, Y. Xiao, Y. Zhao, Z. Zheng, J. Yao, J. Li, *ACS Nano* **2024**, *18*, 27579.
[32] Y. S. Shin, K. Lee, Y. R. Kim, H. Lee, I. M. Lee, W. T. Kang, B. H. Lee, K. Kim, J. Heo, S. Park, Y. H. Lee, W. J. Yu, *Adv. Mater.* **2018**, *30*, 1704435.
[33] H. Xue, Y. Wang, Y. Dai, W. Kim, H. Jussila, M. Qi, J. Susoma, Z. Ren, Q. Dai, J. Zhao, K. Halonen, H. Lipsanen, X. Wang, X. Gan, Z. Sun, *Adv. Funct. Mater.* **2018**, *28*, 1804388.
[34] B. Liu, X. Zhang, J. Du, J. Xiao, H. Yu, M. Hong, L. Gao, Y. Ou, Z. Kang, Q. Liao, Z. Zhang, Y. Zhang, *InfoMat* **2022**, *4*, 12282.
[35] Y. Jiang, R. Wang, X. Li, Z. Ma, L. Li, J. Su, Y. Yan, X. Song, C. Xia, *ACS Nano* **2021**, *15*, 14295.
[36] C. H. Lee, G. H. Lee, A. M. Van Der Zande, W. Chen, Y. Li, M. Han, X. Cui, G. Arefe, C. Nuckolls, T. F. Heinz, J. Guo, J. Hone, P. Kim, *Nat. Nanotechnol.* **2014**, *9*, 676.
[37] Y. Chen, X. Wang, G. Wu, Z. Wang, H. Fang, T. Lin, S. Sun, H. Shen, W. Hu, J. Wang, J. Sun, X. Meng, J. Chu, *Small* **2018**, *14*, 1703293.
[38] M. M. Furchi, A. Pospischil, F. Libisch, J. Burgdörfer, T. Mueller, *Nano Lett.* **2014**, *14*, 4785.
[39] Z. Zou, J. Liang, X. Zhang, C. Ma, P. Xu, X. Yang, Z. Zeng, X. Sun, C. Zhu, D. Liang, X. Zhuang, D. Li, A. Pan, *ACS Nano* **2021**, *15*, 10039.
[40] M. Dai, H. Chen, F. Wang, M. Long, H. Shang, Y. Hu, W. Li, C. Ge, J. Zhang, T. Zhai, Y. Fu, P. Hu, *ACS Nano* **2020**, *14*, 9098.
[41] M. Che, B. Wang, X. Zhao, Y. Li, C. Chang, M. Liu, Y. Du, L. Qi, N. Zhang, Y. Zou, S. Li, *ACS Nano* **2024**, *18*, 30884.
[42] S. Wang, D. Yan, J. I. Michel, A. Corletto, A. A. Wibowo, S. Balendhran, H. Y. Lee, S. Byun, S. Kim, K. B. Crozier, P. C. Sherrell, D. Macdonald, J. Bullock, *ACS Nano* **2024**, *18*, 25046.
[43] J. Ning, Y. Zhou, J. Zhang, W. Lu, J. Dong, C. Yan, D. Wang, X. Shen, X. Feng, H. Zhou, Y. Hao, *Appl. Phys. Lett.* **2020**, *117*, 163104.
[44] Z. Shao, T. Jiang, X. Zhang, X. Zhang, X. Wu, F. Xia, S. Xiong, S. T. Lee, J. Jie, *Nat. Commun.* **2019**, *10*, 1294.
[45] Y. Wang, Z. He, J. Zhang, H. Liu, X. Lai, B. Liu, Y. Chen, F. Wang, L. Zhang, *Nano Res.* **2020**, *13*, 358.
[46] J. Xu, X. Luo, X. Lin, X. Zhang, F. Liu, Y. Yan, S. Hu, M. Zhang, N. Han, X. Gan, Y. Cheng, W. Huang, *Adv. Funct. Mater.* **2024**, *34*, 2310811.
[47] W. Tress, K. Leo, M. Riede, *Phys. Rev. B* **2012**, *85*, 155201.
[48] T. I. Alam, S. U. Hani, S. Ahmed, Y. H. Tsang, *Proc. SPIE* **2024**, *12888*, 128880A.